

Experimental and Theoretical Core Level and Valence Band Analysis of Clean Perovskite Single Crystal Surfaces

Alberto García-Fernández, Sebastian Svanström, Cody M. Sterling, Abhijeet Gangan, Axel Erbing, Chinnathambi Kamal, Tamara Sloboda, Birgit Kammlander, Gabriel J. Man, Håkan Rensmo, Michael Odelius,* and Ute B. Cappel*

A detailed understanding of the surface and interface properties of lead halide perovskites is of interest for several applications, in which these materials may be used. To develop this understanding, the study of clean crystalline surfaces can be an important stepping stone. In this work, the surface properties and electronic structure of two different perovskite single crystal compositions (MAPbI₃ and Cs_xFA_{1-x}PbI₃) are investigated using synchrotron-based soft X-ray photoelectron spectroscopy (PES), molecular dynamics simulations, and density functional theory. The use of synchrotron-based soft X-ray PES enables high surface sensitivity and nondestructive depth-profiling. Core level and valence band spectra of the single crystals are presented. The authors find two carbon 1s contributions at the surface of MAPbI₃ and assign these to MA⁺ ions in an MAI-terminated surface and to MA⁺ ions below the surface. It is estimated that the surface is predominantly MAI-terminated but up to 30% of the surface can be PbI₂-terminated. The results presented here can serve as reference spectra for photoelectron spectroscopy investigations of technologically relevant polycrystalline thin films, and the findings can be utilized to further optimize the design of device interfaces.

their unprecedented multifunctional properties.^[1,2] In 2009 one subclass of perovskites, known as hybrid perovskites, with the general formula ABX₃ revolutionized the optoelectronic field after the discovery of their unprecedented and remarkable optical and electronic properties.^[3] In the ABX₃ structure, A is a monovalent cation, usually methylammonium (MA⁺, CH₃NH₃⁺), formamidinium (FA⁺, CH(NH₂)₂⁺), and/or Cs⁺, B is a divalent cation, usually Pb²⁺ or a mix of monovalent and trivalent cations (e.g., Bi³⁺ and Ag⁺), and X is an anion, usually a halogen or mix of halogens (I⁻, Br⁻, and/or Cl⁻). These materials, specially Pb-based perovskites, have been used, among other applications, in solar cells, now achieving efficiencies over 25%,^[4] in light-emitting diodes with external quantum efficiency exceeding 21%^[5-7] and as photodetectors.^[8,9]

1. Introduction

Since middle of 20th century perovskite materials have been intensively studied by the scientific community because of

Most of the actual perovskite-based optoelectronic devices typically consist of a thin film of a multicrystalline perovskite sandwiched between two selective contacts. Therefore, the interfaces significantly influence the stability and performance of any perovskite-based device. Knowing

A. García-Fernández, T. Sloboda, B. Kammlander, U. B. Cappel
Division of Applied Physical Chemistry
Department of Chemistry
KTH – Royal Institute of Technology
Stockholm SE-100 44, Sweden
E-mail: cappel@kth.se

S. Svanström, G. J. Man, H. Rensmo
Condensed Matter Physics of Energy Materials
Division of X-ray Photon Science
Department of Physics and Astronomy
Uppsala University
Box 516, Uppsala SE-751 20, Sweden

 The ORCID identification number(s) for the author(s) of this article can be found under <https://doi.org/10.1002/sml.202106450>.

© 2022 The Authors. Small published by Wiley-VCH GmbH. This is an open access article under the terms of the Creative Commons Attribution-NonCommercial License, which permits use, distribution and reproduction in any medium, provided the original work is properly cited and is not used for commercial purposes.

DOI: 10.1002/sml.202106450

C. M. Sterling, A. Gangan, A. Erbing, C. Kamal, M. Odelius
Department of Physics
Stockholm University
AlbaNova University Center
Stockholm 10691, Sweden
E-mail: odelius@fysik.su.se

C. Kamal
Theory and Simulations Laboratory
HRDS
Raja Ramanna Centre for Advanced Technology
Indore, Madhya Pradesh 452013, India

C. Kamal
Homi Bhabha National Institute
Training School Complex
Anushakti Nagar, Mumbai, Maharashtra 400094, India

the morphology and composition of the surface of the perovskite is crucial for understanding the interfaces as well as to improve the quality of the contacts which will lead to the fabrication of highly stable and efficient devices.^[10,11]

While most of the existing studies in the literature focus on polycrystalline materials, single crystal hybrid perovskites have also been synthesized and applied in multiple devices.^[12,13] Thanks to their lower defect concentration and their orientation dependent transport behavior, they have shown an improvement in stability, longer carrier diffusion lengths, and low charge recombination rates compared to their polycrystalline counterparts. This makes single crystalline perovskites a very promising candidate for many applications.^[14–16] Accordingly, the growth of high-quality single-crystal perovskite thin films is becoming a great strategy for the fabrication of defect-free perovskite solar cells with photovoltaic parameters close to the theoretical limit.^[17]

Also, despite the huge advances in the design and synthesis of new perovskite compositions as well as in the fabrication of high quality perovskite thin films and thin single crystals, a detailed understanding of perovskite surfaces is still partly lacking, and therefore in a need for further studies.^[18,19] The surface of a semiconductor can be described as the termination of the periodic structure of the crystal lattice which creates the dangling bonds on the surface. Due to the minimization of the surface energy, this process is accompanied by the reconstruction of the atomic structure to saturate dangling bonds, thereby generating specific surface states that deviate from those in the bulk crystal.^[20] For multicrystalline perovskite films, the surface region might be amorphous and contain unreacted perovskite precursors.^[21] To perform studies on clean and crystalline perovskite surfaces, single crystals cleaved under vacuum conditions have to be used. Due to the difficulty of preparing such surfaces, most of surface research was done theoretically. Consequently, there is limited experimental evidence on the atomistic origins of the perovskite-transport layer interface.

Focusing on the simplest possible perovskite composition, the surface termination of the methylammonium lead triiodide (MAPbI₃, CH₃NH₃PbI₃) perovskite has been studied theoretically and experimentally by several groups. Taking into account that the MAPbI₃ surface can be terminated by MAI (CH₃NH₃I) or by PbI₂ (with or without vacancies), Quarti et al. predicted, based on density functional theory (DFT) calculations on a MAPbI₃ (001) surface that a MAI termination is more stable than a PbI₂ termination.^[22] In addition, Haruyama et al. examined, also theoretically, various types of PbI_x terminations on the (100), (101), (110), and (001) surfaces of tetragonal MAPbI₃ finding that vacant termination is more stable than the PbI₂-rich flat one on all the surfaces.^[23] Moreover, She et al. reported an MAI-terminated (001) surface on an epitaxially grown orthorhombic MAPbI₃ film on Au (111) surface,^[24] and in December 2020, Yoshida and coworkers also demonstrated this experimentally by using a combination of ultraviolet photoelectron spectroscopy (UPS) and metastable-atom electron spectroscopy on a MAPbI₃ thin film.^[25]

In addition, it is worth highlighting that the surface termination of several MAPbBr₃ single crystals was experimentally studied. Using a combination of angle resolved photoemission spectroscopy (ARPES) and inverse photoemission spectroscopy,

as well as theoretical modeling, Dowben and coworkers suggested that the termination of MAPbBr₃ single crystals consist on a methylammonium bromide (MABr) layer.^[26] Moreover, Qi and coworkers, using an atomic force microscopy for characterizing an in situ cleaved MAPbBr₃ single crystal, demonstrated a MABr-flat-terminated surface as well.^[27] Despite this, Qi and coworkers were not able to exclude the possibility of the coexistence of a mixture of MABr and PbBr₂ surface terminations and PbBr₂ surface terminations with vacancies.

Photoelectron spectroscopy (PES) is well known as a very powerful technique to investigate electronic and chemical properties of surfaces and interfaces experimentally, as it provides information with elemental sensitivity. PES has been extensively used on the characterization of polycrystalline thin film halide perovskites surfaces, giving information about their chemical composition and also following reactions such as in situ formation and degradation.^[18,21,28–33] However, characterizing halide perovskites surfaces is challenging due to their low stability under ultrahigh vacuum (UHV) conditions, the complexity of the materials itself, and the difficulty of obtain a clean surface for study.^[34] This last challenge was addressed in 2017, when researchers from EPFL cleaved a MAPbBr₃ single crystal under UHV conditions.^[35] Since then, several studies were carried out on cleaved perovskite single crystal surfaces, most of them on MAPbBr₃.^[26,27,36]

In 2020, Iwashita et al. reported the electronic structure of the interface of a MAPbI₃ single crystal and Spiro-OMeTAD.^[37] Very recently we were able to report results for in situ cleaved MAPbI₃ single crystals.^[38,39] Despite that, up to date, studies on perovskite cleaved single crystals have mainly focused on ARPES and UPS and not on core level characterization.^[40–42] As core level studies are a common tool for the characterization of polycrystalline thin films samples, there is a need for a detailed analysis of hybrid perovskites surface composition on clean single crystal surfaces. This analysis could provide a reference for the studies carried out on multicrystalline perovskites with different compositions, where detailed analysis of the organic components can be hindered by surface contamination.

While MAPbI₃ was one of the first hybrid perovskites to be successfully used in solar cells and is by far the most studied, perovskite compositions based on other organic and inorganic cations such as formamidinium (FA⁺, CH₂(NH₂)₂) and cesium (Cs⁺) have been used to improve efficiency and stability of perovskite-based optoelectronic devices by replacing the methylammonium cation.^[43,44] A detailed analysis also of the surface composition of a more complex mixed Cs⁺/FA⁺ perovskite single crystal will therefore be of interest for the application of perovskites in devices.

In this work, we performed synchrotron-based high-resolution soft X-ray PES on clean surfaces of MAPbI₃ (CH₃NH₂PbI₃), Cs_xFA_{1-x}PbI₃ (Cs_x(CH₂(NH₂)₂)_{1-x}PbI₃) and reference PbI₂ single crystals, which were cleaved in situ under UHV. We were able to resolve the details of the C 1s core level of MAPbI₃ and Cs_xFA_{1-x}PbI₃ crystals through varying the photon energy and therefore the probing depth. For MAPbI₃, the C 1s core level of MA⁺ cations is observed at different binding energies for the surface and the bulk of the material, which is supported by theoretical investigations with molecular dynamics (MD) simulations and DFT calculations. In addition, the valence electronic

structures of MAPbI₃ and Cs_xFA_{1-x}PbI₃ were determined with experimental results and DFT calculations pointing to differences in band alignment and chemical bonding.

2. Results and Discussion

Single crystals of MAPbI₃ and black-phase Cs_xFA_{1-x}PbI₃ between 1 and 0.5 cm of diameter were obtained by inverse temperature crystallization. PbI₂ yellow single crystals were synthesized following a cosolvent method previously described by Liu and coworkers.^[45] Crystals of higher cubicity were selected and kept in nitrogen atmosphere and transported to MAX IV to be measured (see Figure S1, Supporting Information, for photos of single crystals). The remaining crystals from the same batch were grounded using a pestle and mortar and characterized by powder X-ray diffraction analysis. As can be seen at Figure S2, Supporting Information, the polycrystalline samples (obtained by grounded single crystals) are a single-phase material with the diffraction peaks in agreement with the profile obtained by single crystal XRD.

The surfaces of MAPbI₃, Cs_xFA_{1-x}PbI₃, and PbI₂ single crystals were characterized by PES using different photon energies (415, 535, and 758 eV) after cleaving the crystals in vacuum. The valence band and Pb 5d, I 4d, Cs 4d, Pb 4f, C 1s, and N 1s core levels were measured. Results obtained using 535 eV photon energy are shown in Figure 1. The binding energies of the perovskites were calibrated against the Fermi level by placing Au 4f_{7/2} measured on an external reference at 84.0 eV. The PbI₂ single crystal showed some charging during measurement and

therefore the binding energies of this crystal were calibrated against Pb 4f_{7/2} set to 138.54 eV. All intensities were normalized to Pb 4f. Figure S3, Supporting Information, shows the N 1s and C 1s Cs_xFA_{1-x}PbI₃ core levels measured before and after the cleaving process. Before cleaving, perovskite N 1s and C 1s core levels were practically impossible to detect due to the high amount of adventitious carbon and extra nitrogen deposited in the surface region of the perovskite single crystal. After the cleaving, we are able to detect narrow and clear peaks corresponding to the perovskite core levels without any extra signals. Moreover, the O 1s core level was also recorded with 758 eV to monitor any possible contamination (Figure S4, Supporting Information). The intensity of O 1s core level signal was below the detection limits of the instrument during all the measurements. Therefore, we can confirm that, after cleaving, we obtained clean perovskite surfaces for the studies.

As can be seen in Figure 1, both position and shape of Pb 4f and Pb 5d core levels spectra are very similar for all three materials. The I 4d spectra confirms the similarities between the two perovskites and the expected difference with PbI₂, where the intensity of I 4d core level is close to 2/3 of that obtained for the perovskites in accordance with their stoichiometry. C 1s and N 1s core levels for the two perovskites samples show clear differences in position, which are expected from the chemical differences between the organic cations. C 1s has a similar intensity for both perovskites and the peak shape is clearly asymmetric for both perovskites. In addition to the expected difference in position, N 1s also shows a clear difference in intensities (Cs_xFA_{1-x}PbI₃ approximately double than MAPbI₃), as expected due to the composition of the organic cations. Formamidinium

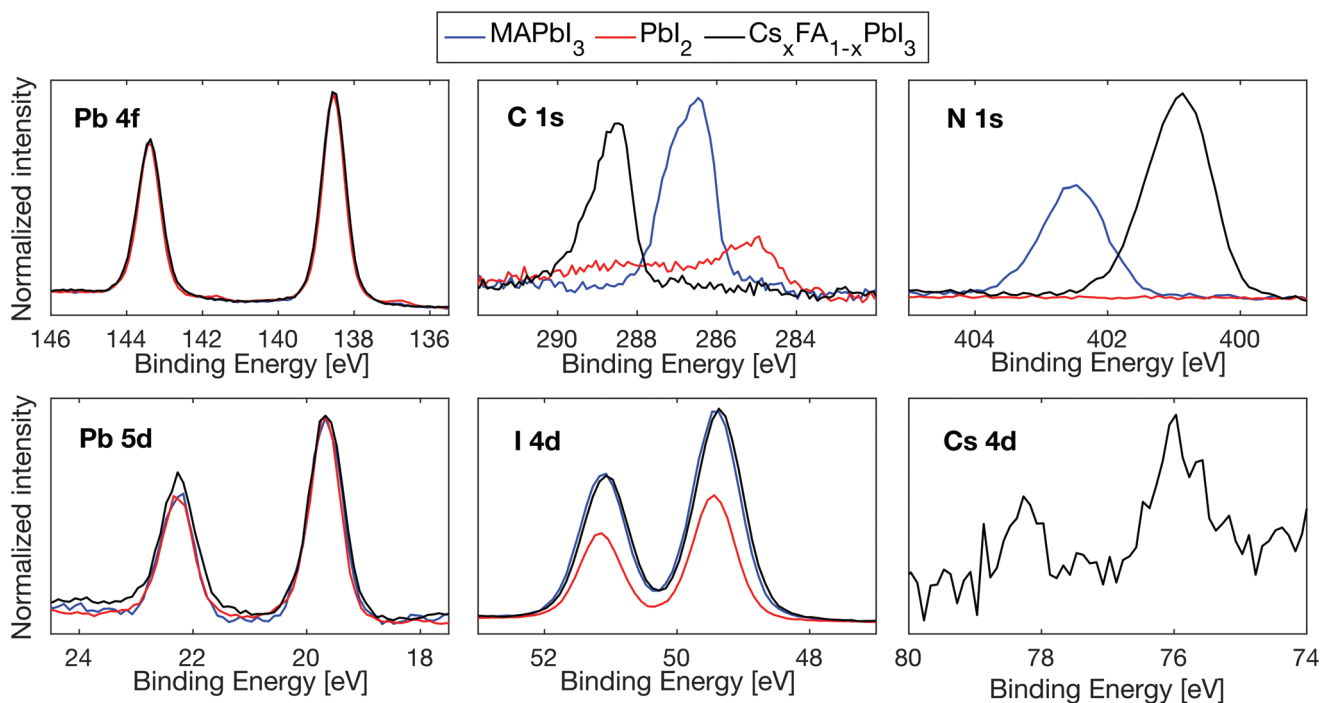


Figure 1. Photoelectron spectra of the Pb 4f, C 1s, N 1s, Pb 5d, I 4d, and Cs 4d core levels recorded from MAPbI₃ (blue line), Cs_xFA_{1-x}PbI₃ (black line), and PbI₂ (red line) single crystals cleaved under vacuum. All core levels were measured using the FlexPES beamline at MAX IV synchrotron with a photon energy of 535 eV. Binding energies of the perovskites were energy calibrated against Au 4f_{7/2} at 84.0 eV while binding energies of PbI₂ were calibrated against Pb 4f_{7/2} at 138.54 eV. All intensities were normalized to Pb 4f.

Table 1. Binding energies positions and standard deviations (SD) in eV, for the core levels of MAPbI₃ and Cs_xFA_{1-x}PbI₃ perovskite and PbI₂ single crystals measured at 535 eV and calibrated against Au 4f_{7/2} (against Pb 4f_{7/2} for PbI₂). The SD represents the uncertainty in the peak position.

	Binding energy positions [$h\nu = 535$ eV]				
	N 1s [eV]	C 1s [eV]	Pb 4f _{7/2} [eV]	I 4d _{5/2} [eV]	Pb 5d _{5/2} [eV]
MAPbI ₃	402.51	286.41 ^{a)}	138.54	49.41	19.67
SD	0.02	0.01	0.01	0.01	0.01
Cs _x FA _{1-x} PbI ₃	400.89	288.54	138.54	49.36	19.66
SD	0.02	0.02	0.01	0.01	0.02
PbI ₂			138.54	49.45	19.68
SD			0.01	0.01	0.01

^{a)}Value for the MA⁺ carbon at lower binding energy (C_L).

is an organic molecule with two nitrogen atoms, while methylammonium has only one nitrogen. In PbI₂, no N 1s or C 1s signal was expected, nevertheless as can be seen in Figure 1, a small amount of adventitious carbon was detected around 285 eV during the measurement, this was due to the difficulty of cleaving PbI₂ single crystals. For Cs_xFA_{1-x}PbI₃, the observation of a Cs 4d signal confirms the presence of Cs in the single crystals.

More detailed core level analysis was obtained using Voigt functions (Figure S5, Supporting Information). The binding energy positions determined from these fits are presented in Table 1. As can be seen in Figure 1, Pb 5d, I 4d, and Pb 4f core levels signals are narrow and curve fitting confirmed the presence of only one spin-orbit doublet with a full width at half maximum (FWHM) below 0.8 eV for all fitted peaks.

The main Pb 4f_{7/2} contribution associated with Pb²⁺ is located at 138.54 eV for both perovskite materials. These positions are similar to those observed in studies on perovskite multicrystalline thin films.^[29,46] For both perovskites, we only detect the Pb²⁺ and do not observe any contribution of metallic lead (Pb⁰), often seen at a binding energy of 137.0 eV.^[28] However, on PbI₂ single crystal a new Pb 4f signal associated with Pb⁰ appears at 137.1 eV, which might form in small amounts due to X-ray exposure.^[47] Analysis of the Pb 5d core level agrees with the analysis of the Pb 4f core level, with very similar binding energy positions for Pb 5d_{5/2} for MAPbI₃, Cs_xFA_{1-x}PbI₃, and PbI₂.

The three compounds show a single I 4d_{5/2} peak with binding energy at 49.41 eV for MAPbI₃, at 49.36 eV for Cs_xFA_{1-x}PbI₃, and at 49.45 eV for PbI₂. These results indicate small differences in the peak separation between I 4d and Pb 4f/Pb 5d for the three materials.

For both perovskites the N 1s core level is wider than the Pb and I core levels (FWHM ≈ 1 eV). Moreover, a small amount of asymmetry had to be included in the peak modeling to obtain a good fit for Cs_xFA_{1-x}PbI₃. Binding energy positions (Table 1) agree well with those reported in literature.^[29,48]

The C 1s core levels are more complex. An accurate modeling of the C 1s peak positions of the organic cations in hybrid lead perovskites are generally highly challenging due to the difficulty of obtaining clean surfaces. The comparison between the single crystal samples before and after cleaving (Figure S3, Supporting Information) shed light on the origin of the C 1s peak

that appears at lower binding energies (around 284.8 eV) for thin film samples and can usually be attributed to adventitious carbon deposited on samples from the preparation environment.^[49–51] However, there have also been several suggestions by the scientific community attributing this signal to C from CH₃NH₂,^[32,49,52] CH₃I,^[32,52,53] or remaining solvents arising from chemicals in the preparation.^[54] Thanks to the cleaving process, we remove all the nonperovskite carbon from the surface of the sample (see Figure 1 and Figure S3, Supporting Information) in a UHV environment, and therefore we detect a clear perovskite C 1s core level. Our C 1s spectrum recorded from clean surfaces of single crystals shows that the dominant spectral contributions from the perovskite material are positioned at >286 eV.

Accordingly, the asymmetry observed in the C 1s can therefore be interpreted as a property of the investigated single crystal perovskite surface. To further examine the origin of the C 1s shape, core-levels at different photon energies were measured. The inelastic mean free path (IMFP), which describes how far an electron on average can travel through a solid before it scatters inelastically, increases with the kinetic energy of the emitted electrons and consequently for a single core level with the energy of the incoming photons.^[55] The probing depth of the experiment, which is responsible for 95% of the signal intensity, is defined as 3 × IMFP. Therefore, by changing the photon energy we were able to change the surface sensitivity of the measurements. The IMFP for the different core electrons at the photon energies used in this study are given in Table S1, Supporting Information.

Before analyzing the effect of surface sensitivity on C 1s, we note that the shape of Pb 4f, Pb 5d, I 4d, and N 1s core levels are the same when comparing data using photon energies of 535 and 758 eV (see Figure 1 and Figure S4, Supporting Information). Moreover, the binding energies are similar with only minor differences in the absolute peak positions (less than 0.05 eV). We therefore used the binding energy positions obtained from both photon energies to calculate the binding energy differences between the different core levels (presented in Table 2). These values can be taken as material constants, as they do not depend on the Fermi level position or on the method of binding energy calibration. They can therefore be used as reference values for future measurements of perovskite-based devices.

Figure 2 shows the C 1s core level spectra for MAPbI₃ and Cs_xFA_{1-x}PbI₃ at different photon energies. No clear changes with photon energy are observed for Cs_xFA_{1-x}PbI₃ except for a small shift in the peak position at 425 eV photon energy.

Table 2. Binding energy differences (in eV) between different perovskite and PbI₂ core levels determined from measurements with photon energies of 535 and 758 eV.

	Energy difference to Pb 4f _{7/2}				Energy difference I 4d _{5/2} -Pb 5d _{5/2}
	N 1s	C 1s	I 4d _{5/2}	Pb 5d _{5/2}	
MAPbI ₃	263.96	147.85 ^{a)}	-89.13	-118.87	29.74
Cs _x FA _{1-x} PbI ₃	262.31	149.98	-89.18	-118.88	29.71
PbI ₂	-	-	-89.1	118.9	29.8

^{a)}Value for the MA⁺ carbon at lower binding energy (C_L).

The FA⁺ C 1s peak could be fitted with a single asymmetric peak to obtain the binding energy position and energy difference to Pb 4f_{7/2} presented in Tables 1 and 2. The asymmetry in the FA⁺ C 1s peak is unaffected by photon energy and has also been observed in more bulk sensitive PES measurements using hard X-ray (photon energies greater than 2000 eV) with a probing depth of more than 11 nm,^[29,56] suggesting that it has to be independent of the surface sensitivity. The origin of this asymmetry should be investigated in future studies, as we are instead focused on the detailed interpretation of the MA⁺ C 1s spectra here. The shape of the MA⁺ C 1s spectra clearly changes continuously as a function of the photon energy. The highest intensity is moved to lower binding energies, as we increase the photon energy, and we are able to distinguish a clear trend in the shape when going from lower photon energies to higher photon energies. The change in peak shape suggests that there are several states contributing to the MA⁺ carbon peak and that the intensity of these varies with photon energy. Additionally, a small amount of adventitious carbon is observed at ≈284.8 eV in particular for the measurement with the most extreme surface sensitivity (415 eV).

Accordingly, the C 1s core level spectra of MAPbI₃ were fitted with several peaks to account for the different types of carbon within the MA⁺ feature. A good fit was obtained at all photon energies when two peaks were used to fit the MA⁺ feature and one peak to account for the small amount of adventitious carbon observed on the samples, which appears with time after cleaving (Figure 3). In this fit, the peak separation between the two MA⁺ peaks was constrained to 0.75 eV at all photon energies and both peaks were fitted with the same FWHM. A clear trend is observed where the relative intensity of the high binding energy peak (C_H) decreases as the photon energy increases and the intensity of the low binding energy peak (C_L) increases. The intensity ratio of the two peaks (C_H/C_L) decreases from 1.11 at 415 eV, to 0.66 at 535 eV and to 0.42 at 758 eV. This trend suggests that the high binding energy MA⁺ peak originates from the surface while the low binding energy MA peak originates from deeper within the sample.

To further investigate the origin of the two types of carbon in MAPbI₃, we performed classical MD simulations to probe the distribution of MA⁺ orientations and surface structures of

the single crystals, as in earlier theoretical studies.^[58] We carried out DFT-based total energy calculations to estimate the relative core-level 1s binding energies, within the Z+1 approximation, of carbon and nitrogen located at the different layers of the perovskite surface slabs. Slab models of different sizes (large and small) were constructed from the crystal coordinates of the tetragonal phase (corresponding system sizes and further details are given in the computational details). Classical MD simulations were performed on both the large and small surface slab models, with both showing closely similar structural results, and thus the smaller size was used for calculations of core level binding energies. Figure 4a shows a snapshot of the large surface structure model of the MAI-terminated MAPbI₃ (001) surface during the MD simulation and Figure 4b represents the distribution of the nitrogen atoms sampled over the simulation. Carbon and nitrogen distributions in other planes can be found in Figure S6, Supporting Information.

The MAI-terminated MD simulations clearly show that the MA⁺ molecules at the surface layer prefer a specific orientation whereby the nitrogen of the molecule points into the surface toward the iodide ions, indicating an interaction between them through N–H ··· I hydrogen bonding and thus influencing the MA⁺ orientation.^[57] There are four iodide ions in the plane surrounding the MA⁺ molecule but, as can be seen in Figure S6, Supporting Information, the N atom of MA⁺ generally points in toward the iodide ions in the underlying PbI₂ layer. Consequently, focusing on surface C atoms, these results show that they point almost exclusively away from the surface. On the other hand, MA⁺ molecules in the layer below the surface present more uniform orientations as it is shown in the lower half of Figure 4b and also in Figure S6, Supporting Information. Overall, our finite temperature classical MD simulations for the MAI-terminated surface show that distributions of MA⁺ molecules at the surface and bulk are distinct with restricted (carbon facing outward) and free rotation of MA⁺, respectively. Thus, the spectral character associated with these types of atoms can be different. However, the PbI₂-terminated surfaces instead show a more equal distribution of externally facing carbon and nitrogen in the outermost layer.^[58]

To probe the above point and support the experimental data, we determine 1s core-level binding energy differences between

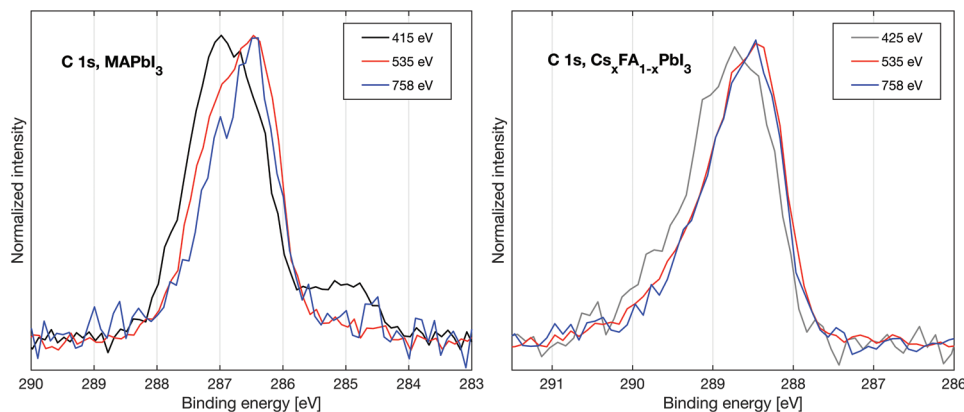


Figure 2. C 1s core level of MAPbI₃ single crystal (left) and Cs_xFA_{1-x}PbI₃ single crystal (right) recorded at different photon energies and energy calibrated against Pb 4f_{7/2} at 138.54 eV.

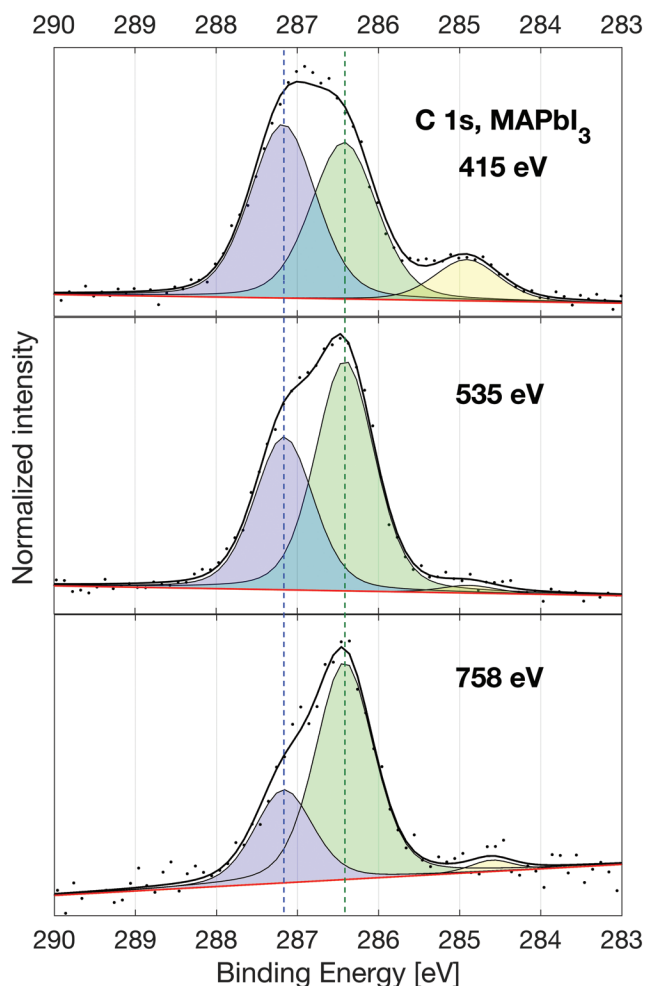


Figure 3. C 1s core level spectra of MAPbI₃ recorded at different photon energies and curve fitted with three contributions: MA⁺ carbon at the surface (C_H, blue), MA⁺ carbon more toward the bulk (C_I, green), and adventitious carbon (yellow).

carbon and nitrogen atoms in MA⁺ molecules in the surface layer and the layer below using DFT-based calculations within the Z+1 approximation, for the small ten-layer models of the MAI- and PbI₂-terminated MAPI surfaces. Surfaces with either carbon or

Table 3. Comparison of Z+1 binding energy differences in MAI-terminated MAPbI₃ systems with C-external surfaces between the surface (S) and S-1 layers for carbon and nitrogen atoms. Positive values indicate a higher binding energy on the surface compared to S-1.

Surface MA ⁺ orientation	C S → S-1 shift [eV]	N S → S-1 shift [eV]	C–N difference [eV]
C-external	0.85	−0.03	0.88
C-external flipped S-1	1.12	0.20	0.92

nitrogen facing out (external) from the surface were optimized using the MYP1 force-field, and further MAI-terminated surfaces were created by re-optimization after flipping the MA⁺ orientation in the first inner layer from the surface (S-1). This creates a total of four MAI-terminated surfaces (C-external, C-external with S-1 flipped, N-external, and N-external with S-1 flipped) and 2 PbI₂-terminated surfaces (C-external and N-external). The optimized geometries for the carbon-external MAI-terminated system are shown in Figure S7, Supporting Information.

The results of the Z+1 calculations for these six systems and the difference in binding energy between the surface (S) and the S-1 atoms are given in Tables 3 and 4 for the MAI-terminated systems and Table 5 for the PbI₂-terminated systems. Both the C- and N-external MAI-terminated results show a significant S → S-1 difference for carbon but not for nitrogen, which is in accordance with the experimental results. Conversely, the PbI₂-terminated surfaces do not show this difference, indicating that such a surface should not cause a binding energy difference in the C 1s core levels.

According to the results shown in Figure 4b, the MAI-terminated MAPbI₃ surface shows almost exclusively the carbon pointing outwards from the surface as opposed to the nitrogen, while the inner layers are more homogeneous in the MA⁺ orientation. Therefore, those geometries which have the carbon atom outwards on the surface layer (Table 3) should be considered more likely than the others, and these results closely match the experimental observation of a >0.7 eV shift between two types of carbon as seen in Figure 3.

The theoretical modeling of the MAPbI₃ surface presented here therefore suggests that carbon atoms in the MA⁺ molecules in the surface layer of the MAI-terminated MAPbI₃ crystal should appear at a higher binding energy than those in the layer below the surface. This large difference in binding energy

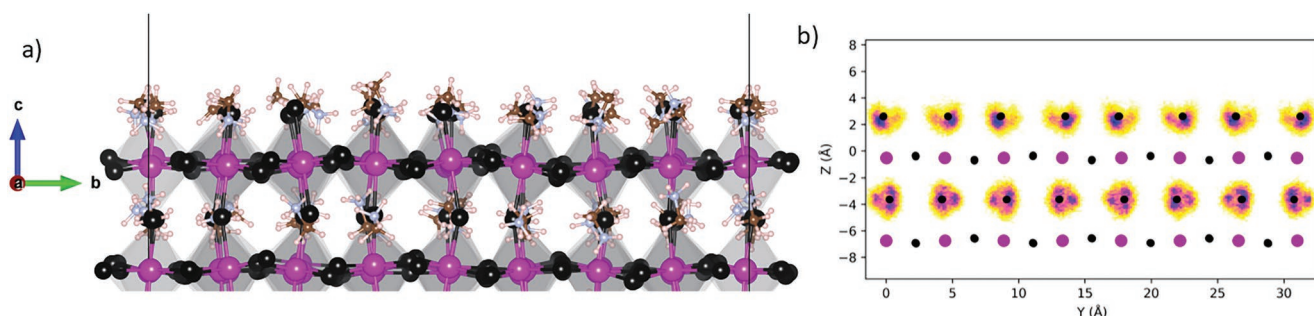


Figure 4. a) Snapshot of the YZ plane (a side view) of the surface structure during the MD simulation of the large model of the MAI-terminated MAPbI₃ structure. The purple sphere represents Pb, black is I, light blue is N, brown is C, and pink spheres represent H atoms. b) Spatial distribution of N atoms displayed against the inorganic framework in the YZ plane for the top two MAI layers along with Pb–I sublattice for MAI-terminated MAPbI₃ structure. Intensity of the color of the distribution refers to the average density.

Table 4. Comparison of Z+1 binding energy differences in MAI-terminated MAPbI₃ systems with N-external surfaces between the surface (S) and S-1 layers for carbon and nitrogen atoms. Positive values indicate a higher binding energy on the surface layer compared to S-1.

Surface MA ⁺ orientation	C S → S-1 shift [eV]	N S → S-1 shift [eV]	C–N difference [eV]
N-external	0.88	0.23	0.65
N-external flipped S-1	0.64	0.15	0.49

is, however, not observed for the corresponding nitrogen atoms. Furthermore, this difference is also not observed for the PbI₂-terminated surfaces. These results are in agreement with the experimental findings, where a significant separation between surface and not-surface peaks is only observed for carbon but not nitrogen. We can therefore assign the high binding energy C 1s peak seen in Figure 3 to carbon in MA⁺ molecules at the MAI-terminated surface.

If we assume that all carbon atoms sitting in the MAI surface layer appear at the higher binding energy and all carbon atoms in MA⁺ molecules in other layers appear at the lower binding energy, we can use IMFP values to estimate the expected intensity ratios between the two peaks and compare these to the experimental ones. IMFP values estimated by the TPP-2M method^[59] (see Experimental Section for details) are given in **Table 6**. Using these values and a distance of 0.63 nm between MA⁺ molecules in different crystal layers,^[60] we can estimate the relative intensities which carbon atoms in different layers of the single crystal should contribute to the photoelectron spectra. We then divide the intensity of the first layer (termed C_{surf}) by the sum of all other layers (termed as C_{bulk}) (Table 6). Given the distinction made between the carbon in surface MA⁺ and MA⁺ in other layers of the crystal, these ratios should correspond to the experimental $C_{\text{h}}/C_{\text{l}}$ ratios for a surface with 100% MAI termination. As can be seen in Table 6, the calculated ratios are significantly higher than experimental ones. This suggests that not all of the surface is MAI-terminated. We therefore also calculate the intensities for a PbI₂-terminated surface, in which the first MA⁺ layer is found at half the distance of one layer below the surface. As we do not expect changes in binding energy for the different layers in a PbI₂-terminated surface, we calculate all intensities from PbI₂-terminated regions toward C_{bulk} according to the following equation:

$$\frac{C_{\text{surf}}}{C_{\text{bulk}}} = \frac{C_{\text{surf}}(\text{MAI}) \cdot f(\text{MAI})}{C_{\text{bulk}}(\text{MAI}) \cdot f(\text{MAI}) + C(\text{PbI}_2) \cdot (1 - f(\text{MAI}))} \quad (1)$$

Table 5. Comparison of Z+1 binding energy differences in PbI₂-terminated MAPbI₃ systems between the surface (S) and S-1 layers for carbon and nitrogen atoms. Positive values indicate a higher binding energy on the surface layer compared to S-1.

Outermost [S] MA ⁺ orientation	C S → S-1 shift [eV]	N S → S-1 shift [eV]	C–N difference [eV]
C-external	−0.28	0.01	−0.29
N-external	−0.19	−0.33	0.14

Table 6. Inelastic mean free path of photoelectrons emitted from the C 1s core level with different photon energies and experimental and theoretical intensity ratios between different types of carbon.

$h\nu$ [eV]	IMFP C 1s [nm]	$C_{\text{h}}/C_{\text{l}}$ [exp]	$C_{\text{surf}}/C_{\text{bulk}}$, 100% MAI termination	$C_{\text{surf}}/C_{\text{bulk}}$, 72% MAI termination
415	0.61	1.11	1.83	1.11
535	0.87	0.66	1.06	0.68
758	1.34	0.42	0.61	0.41

where f is the fraction of the surface, which is MAI-terminated. The best agreement of $C_{\text{surf}}/C_{\text{bulk}}$ with the experimental $C_{\text{h}}/C_{\text{l}}$ ratio is obtained at $f = 0.72$ (Table 6). This suggests that although the cleaved surface is mostly MAI-terminated, there could also be a significant fraction, which is PbI₂-terminated or where MA molecules are missing from the surface.

Further insights into the surface composition can be gained through the quantitative analysis of the different core level intensities. This analysis is particularly meaningful, as we perform the studies on UHV-cleaved single crystals and we are able to obtain clean surfaces to analyze. The analysis was first performed assuming homogeneous materials and using tabulated cross sections. However, as described previously, the obtained atomic density is very weighted toward the surface due to the exponential decrease in the escape probability of the photoelectrons. This will affect the values obtained for nonhomogeneous materials, where the most surface dominant species will show higher relative atomic percentages. Table S2, Supporting Information, summarizes the ratios for the perovskite and PbI₂ single crystals. Considering that PbI₂ is a starting material for the synthesis of hybrid perovskites, it was used as a reference, obtaining a I 4d/Pb 5d ratio of 2.10 at 535 eV and 2.05 at 758 eV, which are very close to the theoretical ratio of 2.

The ratios of both perovskite materials were then normalized against the PbI₂ ratio set to two and are presented in Table 7. Values obtained from analysis of the Pb 4f and Pb 5d core levels are relatively similar. Both perovskites show I/Pb ratios, which are somewhat higher than the ratio expected from stoichiometry (3.0), in particular with the more surface sensitive photon energy (535 eV). With the higher photon energy, the measurement is more bulk sensitive and the ratio is closer to the expected bulk value.

Quantification of carbon and nitrogen is more complicated, as we do not have a reference sample and at the low photon energies used here, there are significant differences in probing depth for Pb 4f, C 1s, and N 1s core levels. However, we can compare the values obtained for MAPbI₃ and Cs_xFA_{1-x}PbI₃ (see Table S2, Supporting Information). We observe higher C/Pb ratios for MAPbI₃ than for Cs_xFA_{1-x}PbI₃. This difference can partially be related to the replacement of some FA⁺ cations by Cs⁺. However, quantification of the Cs 4d core level suggests that the amount of Cs⁺ in the crystal is very low (4% relative to lead) but enough to stabilize the formamidinium lead iodide in its cubic phase (black color). Moreover, C 1s/N 1s ratios were also calculated and shown in Table 7. To be able to do a comparison between both perovskites, one has to remember that FA⁺ contains two nitrogen atoms while MA⁺ contains only one. That more of the carbon is observed relative to nitrogen

Table 7. Ratios of I 4d/Pb 4f and I 4d/Pb 5d core levels of MAPbI₃ and Cs_xFA_{1-x}PbI₃ single crystals normalized against PbI₂ single crystal and C 1s/N 1s not normalized.

Compound	<i>hν</i> [eV]	Normalized against PbI ₂		Not normalized C 1s/N 1s
		I 4d/Pb 4f	I 4d/Pb 5d	
MAPbI ₃	535	3.40	3.54	1.26
	758	3.15	3.32	1.34
Cs _x FA _{1-x} PbI ₃	535	3.39	3.47	0.54
	758	3.22	3.17	0.58

than expected for stoichiometry is consistent with the higher probing depth for the C 1s core level compared to the N 1s for the same photon energy. For Cs_xFA_{1-x}PbI₃, the ratios are closer to those expected from stoichiometry. The ratios obtained for MAPbI₃ are higher, suggesting that relatively more carbon of the cation is observed for MA⁺ than for FA⁺. This could be related to the preferred orientation of the MA⁺ molecules with the carbon pointing away from the surface demonstrated by the MD simulation. This preferred orientation could increase the intensity of the observed carbon relative to nitrogen.

In addition to the core level results discussed above, the valence band region of both perovskites was measured using different photon energies. **Figure 5** shows a comparison between the valence band region of both perovskites at 758 and 130 eV. All spectra were calibrated and normalized against Pb 5d at 19.67 eV for MAPbI₃ and 19.66 eV for Cs_xFA_{1-x}PbI₃. At the higher photon energy (758 eV, **Figure 5** right), the valence band region of both perovskites is very similar. At photon energy above 500 eV, the valence band region is dominated by the inorganic framework of the perovskite due the relatively higher photoionization cross sections of the orbitals of the iodide and lead than those of nitrogen and carbon.^[61] Therefore, in the measured spectra, we observe the Pb 5d core level and the main valence band feature which mostly involves inorganic states.

At lower photon energies (**Figure 5** left and **Figure 6**), additional features are observed at binding energies between 4 and 18 eV, which vary between the two different perovskites. To rationalize these differences and assign spectral features, we compare the experimental spectra recorded at different photon

energies to calculated densities of states (**Figure 6**). This comparison can be used to understand the origin of the splitting of the main valence feature at about 5.5 eV for lower photon energies, as the photoionization cross section of N is significantly larger in this case. The main valence band feature in both MAPbI₃ and Cs_xFA_{1-x}PbI₃, primarily consists of anti-bonding I 5p-states and Pb 6s-states, results in accordance with previous studies of these systems.^[61,62] The feature observed at ≈5.5 eV with low photon energies for the case of Cs_xFA_{1-x}PbI₃ perovskite can be assigned to a considerable contribution from N 2p. The calculated position of this N 2p peak, seen in blue at 4.5 eV in **Figure 6** right, is slightly lower in binding energy compared to the experiments. This can however be attributed to approximations within our theoretical models. This contribution is missing in the MAPbI₃ PDOS and the corresponding splitting with lower photon energies is not seen experimentally (**Figure 5** left). Instead, a feature is observed at ≈11 eV both experimentally and in theoretical models (**Figure 6**, left), which can be assigned to N 2p in MAPbI₃. The effect of Cs⁺ at the displayed binding energies is minimal with only a small intensity contribution at 10 eV suggesting that Cs only has a marginal effect on the valence electronic structure.

3. Conclusion

We were successfully able to synthesize black MAPbI₃ and Cs_xFA_{1-x}PbI₃ perovskite single crystals and prepare clean surfaces by cleaving them under vacuum conditions. The surfaces were characterized using high-resolution soft X-ray PES with synchrotron radiation and the results were compared to orientational distributions obtained from classical MD simulations and to DFT calculations of surface shifts in the N 1s and C 1s core level binding energies and of the valence band.

The core level positions, binding energy differences, and valence band spectra presented for the clean surfaces of MAPbI₃ and Cs_xFA_{1-x}PbI₃ provide useful materials references for the large number of studies, which use PES as a tool for the characterization of perovskites. Quantification of the core level intensities was carried out at 535 and 758 eV and suggests a slightly iodide-rich surface for both types of perovskites

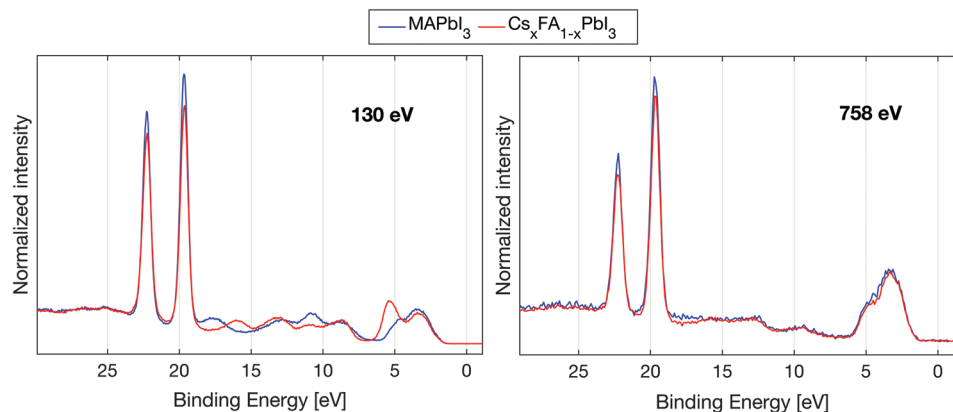


Figure 5. Valence band region of MAPbI₃ (blue line) and Cs_xFA_{1-x}PbI₃ (red line) perovskites at 130 eV (left) and 758 eV (right). All the spectra were energy-calibrated Pb 5d (19.67 eV for MAPbI₃ and 19.66 eV for Cs_xFA_{1-x}PbI₃) and intensity normalized against the fitted Pb 5d area.

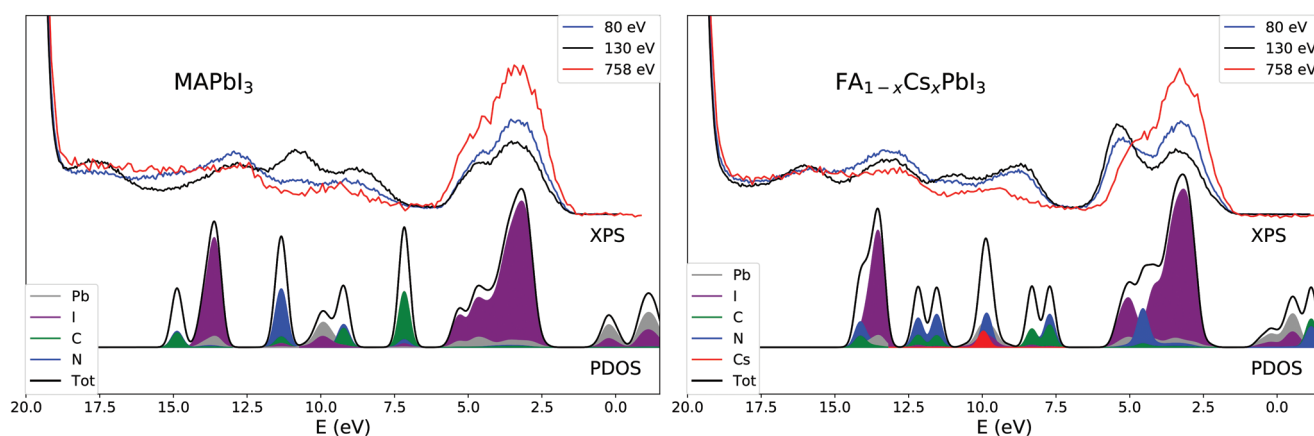


Figure 6. Comparison between the experimental data (top lines) and the PDOS data (bottom) of the valence band region of MAPbI₃ (left) and Cs_xFA_{1-x}PbI₃ (right) perovskites measured at different photon energies: 80 eV (blue line), 130 eV (black line), and 758 eV (red line). Experimental data was calibrated and normalized against Pb 5d at 19.67 eV for MAPbI₃ and 19.66 eV for Cs_xFA_{1-x}PbI₃.

in agreement with a surface which is mostly terminated by the iodide salts of the organic cations.

Due to the success in preparing clean single crystal surfaces, it was possible to investigate in detail the C 1s core level and we found that the shape of the MAPbI₃ C 1s spectra clearly changed as a function of the photon energy. Experimentally, we were able to distinguish two peaks with the higher binding energy peak becoming relatively more intense when using lower photon energies, that is, at higher surface sensitivity. Through DFT-based binding energy calculations within Z+1 approximation, we were able to assign the higher binding energy peak to MA⁺ molecules in an MAI-terminated surface, while the lower binding energy peak can be assigned to all other MA⁺ molecules. Using the assignment of carbon peaks, we modeled the relative intensities of the two C 1s peaks at the different photon energies using the IMFP and surface models with MAI and PbI₂ termination. This modeling suggests that the surface is mostly MAI-terminated, but there could also be a significant fraction, which is PbI₂-terminated. Such effect in the MA⁺ ion is not observed for the N 1s core-levels.

For Cs_xFA_{1-x}PbI₃, we observe a significant asymmetry in the FA⁺ C 1s signal, which is unaffected by photon energy and has also been observed in measurements with photon energies above 2000 eV,^[29,56] suggesting that it is independent of the surface but rather inherent to the organic cation. Further investigations are needed to understand the origin of this asymmetry.

In agreement with previous investigations on thin film perovskites, it was found that mostly the contributions of the inorganic framework to the valence band of the perovskite are probed with high photon energies. However, at lower photon energies we were able to observe clear differences in the extended valence band structure due to the organic cations. Valence band calculations give an explanation for the valence band splitting around 5.5 eV in FA-based perovskites.

Our findings not only provide reliable references for core level and valence band spectra as well as core-to-core level energy differences for commonly used perovskites, but also pave the way for extending the knowledge of perovskite surfaces, which is very important for understanding reaction

mechanism on interfaces and therefore, create more stable, and efficient perovskite-based operational devices.

4. Experimental Section

Synthesis of MAPbI₃ Single Crystals: MAPbI₃ (CH₃NH₃PbI₃) single crystals with a diameter of about 1 cm were obtained by inverse temperature crystallization. A 1 M solution of MAI (CH₃NH₃I) (Sigma-Aldrich) and PbI₂ (TCI) was prepared in γ -butyrolactone (GBL) stirring at room temperature. After the precursors were completely dissolved, 1.5 mL of the final solution was filtered through a 0.45 μ m PTFE filter and transferred to a 3 mL open glass vial. Subsequently the vial was heated up to 100 °C. After 1 h, selected seed crystals were collected and carefully placed in several new glass vials containing filtered solution and heated up to 100 °C (only one crystal in each new vial). The selected crystal grew in size. The process was repeated as many times as it was necessary until the desired size was obtained.

Synthesis of Cs_xFA_{1-x}PbI₃ Single Crystals: Cs_xFA_{1-x}PbI₃ (Cs_x(CH₂(NH₂)₂)_{1-x}PbI₃) single crystals with a diameter of about 0.5 cm were obtained by inverse temperature crystallization. A 1 M solution of formamidinium iodide (CH₂(NH₂)₂) (Sigma-Aldrich) and lead iodide (PbI₂) (TCI) was prepared in γ -butyrolactone (GBL) stirring at room temperature. After the precursors were completely dissolved, 0.1 M of CsI was added to the solution and it was stirred at room temperature until a yellow transparent solution was obtained. After that, 1.5 mL of the final solution was filtered through a 0.45 μ m PTFE filter and transferred to a 3 mL open glass vial. Subsequently the vial was heated up to 100 °C. After 1 h, selected seed crystals were collected and carefully placed in several new glass vials containing filtered solution and heated up to 100 °C (only one crystal in each new vial). The selected crystal grew in size. The process was repeated as many times as it was necessary until the desired size was obtained.

Synthesis of PbI₂ Single Crystals: PbI₂ single crystals with a diameter of around 0.1 cm were synthesized following a cosolvent method previously described by Liu and coworkers,^[45] where 2.35 g of benzylamine hydroiodide (in-house synthesized, description below) was used as cosolvent in a solution of 4.61 g of PbI₂ (TCI) in 10 mL of GBL. The solution was heated and stirred during 1 h at 7 °C. After that, the solution was filtered through a 0.45 μ m PTFE filter and transferred into a 20 mL PTFE-lined hydrothermal synthesis autoclave reactor and maintained at 180 °C during 7 days for crystallization. After 7 days, PbI₂ single crystals were obtained.

Benzylamine Hydroiodide Synthesis: The benzylamine (C₆H₅CH₂NH₂) solution (Sigma Aldrich) in a slight excess was reacted with hydriodic

acid (Sigma Aldrich) in an ice bath and under vigorous stirring. The crystallization of benzylamine hydroiodide was achieved using a rotary evaporator. The obtained microcrystals were washed with absolute diethyl ether several times and finally dried in a vacuum line overnight.

Photoelectron Spectroscopy Measurements and Analysis: The samples were measured at FlexPES beamline at MAX IV facility placed in Lund, Sweden. The X-rays were generated by a linear polarized undulator with a period length of 54.4 mm and monochromated using a plane grating monochromator (modified Zeiss SX700). A defocused beam was used to reduce beam damage and the X-ray intensity was controlled by adjusting the exit slit to 20 μm for 758 eV and to 10 μm for all the other used photon energies (80, 130, 415, and 535 eV). Photoelectrons were detected by a Scienta SES-2002 spectrometer in normal emission from the samples. The step size of the measurements was 0.1 eV and the pass energy was 50 eV for the valence band characterization at 80, 130, and 100 eV for the rest of the core levels characterization.

Single crystals were mounted on sample plates using EPO-TEK H20E two component epoxy and heated up to 100 °C during 1 h until the epoxy was cured. This process was done in air at ambient conditions. Subsequently, the sample plates were introduced in a vacuum chamber and cleaved under a pressure of around 10^{-8} mbar and immediately transferred to the main analysis chamber, where measurements were carried out at 10^{-10} mbar.

The photoelectron spectra of the core levels were fitted using a pseudo-Voigt function^[63] with a linear or Herrera-Gomez^[64] background as needed. The Lorentzian contributions for the investigated core levels were small (<0.3 eV) and were kept fixed at the same width for the fitting of one core level. To estimate the ratios between elements, the area of the photoelectron peaks was normalized to the photoionization cross section.^[65] For fitting the C 1s and N 1s signal of FA⁺, an asymmetrical peak shape was used.^[66] The standard deviation of the peak positions were estimated from repeat measurements.

IMFPs for electrons emitted from the C 1s core levels of MAPbI₃ were estimated using the TPP-2M equation.^[59] A bandgap of 1.55 eV,^[67] a molecular weight of MAPbI₃ of 620 g mol⁻¹, a number of valence electrons of 40,^[68] and a density of 4.16 g cm⁻³ was used in the calculations.^[69]

Computational Details: The CP2K code^[70] was employed to perform the classical MD simulations and the calculations of the core level binding energy shifts and the valence band density of state within density function theory. The structural models were designed based on experimental structure of MAPbI₃ and FAPbI₃.^[60,69]

Molecular Dynamics Simulations: MD simulations were carried out in order to study the MAPbI₃ surfaces. The (001) plane was used to generate the structures for both MAI and PbI₂ terminations.^[24] A 48 atom unit cell of MAPbI₃ in the tetragonal phase was used to construct the larger surface structure supercell.^[60] In a large slab model, the unit cell was multiplied four times in the x and y directions and appropriately in the z direction to get 20 units of MAI layers in the supercell for sufficiently thick slabs, with a total of 640 MA molecules in the super cell. The dimensions of the supercell were 3.6 nm in the x and y directions and 15.1 nm in the z direction. The surfaces had a thickness of around 12.6 nm, and the remaining 2.5 nm was a vacuum region used to avoid interaction between the periodic surface images in the z direction. Both the MAI- and PbI₂-terminated layers were symmetric around the middle PbI₂ layer and the termination was kept the same for both the bottom and top layers. In all the simulations the periodic boundary conditions were taken into account. Simulations were also performed on a small model multiplied two times in the x and y directions and with ten units of MAI layers in the slab, which gave the same results on orientation of MA molecules and was used in DFT Z+1 calculations.

The MYP1 model^[71] was used to describe the interactions between the atoms and the organic and inorganic framework. This classical force-field had been previously used for the simulation of MAPbI₃ bulk and as well as surfaces with different terminations. The simulations were carried out for 100 ps in the NVT ensemble using a timestep of 0.5 fs. Temperature was maintained at 300 K using a four-chain Nosé-Hoover thermostat.^[72-74] A cutoff of 12 Å was used for the nonbonded

parameters in the MYP1 force-field. The structures were visualized using the VESTA software.^[75]

Core Level Binding Energy and Valence Band Calculations: MAI- and PbI₂-terminated MAPI surfaces were created from the small model used in the MD simulations with ten layers of MA⁺ molecules.^[60] First, perfect crystalline structures were formed with either the MA⁺ carbon or nitrogen oriented from the central layer of PbI₂ out external from the surface. These surfaces were then cell optimized using the MYP1 force-field, with the constraints that the vertical cell parameter was fixed to leave ≈ 25 Å vacuum between periodic surface images and the central PbI₂ layer was fixed in their Z coordinates, shown in Figure S7a, Supporting Information, for the carbon-external MAI-terminated system. For the MAI-terminated systems, the cell-optimized structures had the MA⁺ ions of the first layer in from the surface (S-1) flipped by 180° and the cell re-optimized to investigate the effect of orientation on the results, shown in Figure S7b, Supporting Information.

The N 1s and C 1s core level binding energy shifts of different atomic sites in the structures were calculated within the Z+1 approximation by replacing an individual carbon/nitrogen atom with a nitrogen/oxygen atom in separate calculations and comparing the total energy difference for different atomic size to estimate the core level binding energy shift. The Z+1 approximation was used here as opposed to explicit depopulation of the core level because it was faster and gave similar results for the relative differences that were of interest in this study. Due to the symmetry of the geometries, only one MA⁺ molecule in each layer needed to be calculated. Calculations were performed under the GAPW formalism^[76] with the PBE exchange-correlation functional,^[77] Grimme's D3 pairwise dispersion correction,^[78,79] and a multigrid with five grids and a cutoff of 600 Rydberg. Each atom was calculated using Goedecker-Teter-Hutter (GTH) pseudopotentials and the corresponding basis sets: TZVP-MOLOPT-GTH for the MA⁺ atoms and TZVP-MOLOPT-SR GTH for Pb and I atoms.^[80-82]

The valence band calculations and the corresponding optimized geometries of both MAPbI₃ and Cs_xFA_{1-x}PbI₃ were also calculated at the same level of theory as the Z+1 calculations but using the conventional GPW method^[83] instead of the GAPW formalism.

Supporting Information

Supporting Information is available from the Wiley Online Library or from the author.

Acknowledgements

The authors acknowledge funding from the Swedish Research Council (Grant Nos. VR 2018-04125, VR 2018-06465 and VR 2018-04330), the Göran Gustafsson Foundation, the Swedish Foundation for Strategic Research (Project No. RMA15-0130), and the Carl Tryggers Foundation (Grant No. CTS 18:59). The authors acknowledge MAX IV Laboratory for time on Beamline FlexPES under proposal 20200451. Research conducted at MAX IV, a Swedish national user facility, was supported by the Swedish Research Council under contract 2018-07152, the Swedish Governmental Agency for Innovation Systems under contract 2018-04969, and Formas under contract 2019-02496. The authors also thank Stephan Appelfeller, Alexei Preobrajenski, and Alexander Generalov for support during the FlexPES beamtime. M.O. acknowledges support from the Swedish Energy Agency (Grant No. 2017-006797). The calculations were enabled by resources provided by the Swedish National Infrastructure for Computing (SNIC), partially funded by the Swedish Research Council through Grant Agreement No. 2018-05973.

Conflict of Interest

The authors declare no conflict of interest.

Data Availability Statement

Research data are not shared.

Keywords

molecular dynamics, perovskite single crystals, soft X-ray photoelectron spectroscopy, synchrotron radiation, Z+1 calculation

Received: October 31, 2021

Published online: February 5, 2022

- [1] A. S. Bhalla, R. Guo, R. Roy, *Mater. Res. Innovations* **2000**, 4, 3.
- [2] A. García-Fernández, E. J. Juárez-Pérez, S. Castro-García, M. Sánchez-Andújar, A. Señaris-Rodríguez, in *Perovskites and Other Framework Structure Crystalline Materials*, **2021**, pp. 134–174.
- [3] C. N. R. Rao, A. K. Cheetham, A. Thirumurugan, *J. Phys.: Condens. Matter* **2008**, 20, 159801.
- [4] NREL, Best Research-Cell Efficiency Chart, <https://www.nrel.gov/pv/cell-efficiency.html> (accessed: July 2021).
- [5] T. Chiba, Y. Hayashi, H. Ebe, K. Hoshi, J. Sato, S. Sato, Y. Pu, S. Ohisa, J. Kido, *Nat. Photonics* **2018**, 12, 681.
- [6] T. Fang, T. Wang, X. Li, Y. Dong, S. Bai, J. Song, *Sci. Bull.* **2021**, 66, 36.
- [7] D. Kang, S. Kim, Y. C. Kim, I. T. Han, H. J. Jang, J. Y. Lee, N. Park, *ACS Energy Lett.* **2020**, 5, 2191.
- [8] M. Ahmadi, T. Wu, B. Hu, *Adv. Mater.* **2017**, 29, 1605242.
- [9] Y. Liu, Y. Zhang, X. Zhu, J. Feng, I. Spanopoulos, W. Ke, Y. He, X. Ren, Z. Yang, F. Xiao, K. Zhao, M. Kanatzidis, S. Liu, *Adv. Mater.* **2021**, 33, 2006010.
- [10] L. Qiu, S. He, L. K. Ono, Y. Qi, *Adv. Energy Mater.* **2020**, 10, 1902726.
- [11] D. Niesner, *APL Mater.* **2020**, 8, 090704.
- [12] B. Turedi, V. Yeddu, X. Zheng, D. Y. Kim, O. M. Bakr, M. I. Saidaminov, *ACS Energy Lett.* **2021**, 6, 631.
- [13] J. Li, Z. Han, Y. Gu, D. Yu, J. Liu, D. Hu, X. Xu, H. Zeng, *Adv. Funct. Mater.* **2021**, 31, 2008684.
- [14] X. Cheng, S. Yang, B. Cao, X. Tao, Z. Chen, *Adv. Funct. Mater.* **2020**, 30, 1905021.
- [15] Y. Lei, Y. Chen, R. Zhang, Y. Li, Q. Yan, S. Lee, Y. Yu, H. Tsai, W. Choi, K. Wang, Y. Luo, Y. Gu, X. Zheng, C. Wang, C. Wang, H. Hu, Y. Li, B. Qi, M. Lin, Z. Zhang, S. A. Dayeh, M. Pharr, D. P. Fenning, Y. H. Lo, J. Luo, K. Yang, J. Yoo, W. Nie, S. Xu, *Nature* **2020**, 583, 790.
- [16] X. Jiang, X. Fu, D. Ju, S. Yang, Z. Chen, X. Tao, *ACS Energy Lett.* **2020**, 5, 1797.
- [17] Y. Liu, Y. Zhang, X. Zhu, Z. Yang, W. Ke, J. Feng, X. Ren, K. Zhao, M. Liu, M. G. Kanatzidis, S. Liu, *Sci. Adv.* **2021**, 7, eabc8844.
- [18] P. Schulz, D. Cahen, A. Kahn, *Chem. Rev.* **2019**, 119, 3349.
- [19] J. Xue, R. Wang, Y. Yang, *Nat. Rev. Mater.* **2020**, 5, 809.
- [20] S. G. Davison, M. Stęszlicka, *Basic Theory of Surface States*, Oxford University Press, New York **1996**.
- [21] B. Philippe, G. J. Man, H. Rensmo, in *Characterization Techniques for Perovskite Solar Cell Materials* (Eds: M. Pazoki, A. Hagfeldt, T. Edvinsson), Elsevier, New York **2019**, pp. 109–137.
- [22] C. Quarti, F. De Angelis, D. Beljonne, *Chem. Mater.* **2017**, 29, 958.
- [23] J. Haruyama, K. Sodeyama, L. Han, Y. Tateyama, *J. Phys. Chem. Lett.* **2014**, 5, 2903.
- [24] L. She, M. Liu, D. Zhong, *ACS Nano* **2016**, 10, 1126.
- [25] A. Mirzehmet, T. Ohtsuka, S. A. Syed, T. Yuyama, P. Krüger, H. Yoshida, *Adv. Mater.* **2021**, 33, 2004981.
- [26] T. Komesu, X. Huang, T. R. Paudel, Y. B. Losovyj, X. Zhang, E. F. Schwier, Y. Kojima, M. Zheng, H. Iwasawa, K. Shimada, M. I. Saidaminov, D. Shi, A. L. Abdelhady, O. M. Bakr, S. Dong, E. Y. Tsybal, P. A. Dowben, *J. Phys. Chem. C* **2016**, 120, 21710.
- [27] J. I. J. Choi, M. E. Khan, Z. Hawash, H. Lee, L. K. Ono, Y. Qi, Y. H. Kim, J. Y. Park, *J. Phys. Chem. C* **2020**, 124, 1484.
- [28] B. Philippe, B. W. Park, R. Lindblad, J. Oscarsson, S. Ahmadi, E. M. J. Johansson, H. Rensmo, *Chem. Mater.* **2015**, 27, 1720.
- [29] B. Philippe, M. Saliba, J. P. Correa-Baena, U. B. Cappel, S. H. Turren-Cruz, M. Grätzel, A. Hagfeldt, H. Rensmo, *Chem. Mater.* **2017**, 29, 3589.
- [30] U. B. Cappel, V. Lanzilotto, E. M. J. Johansson, T. Edvinsson, H. Rensmo, in *Molecular Devices for Solar Energy Conversion and Storage* (Eds: H. Tian, G. Boschloo, A. Hagfeldt) Springer, Singapore **2018**, pp. 433–476.
- [31] J. Endres, M. Kulbak, L. Zhao, B. P. Rand, D. Cahen, G. Hodes, A. Kahn, *J. Appl. Phys.* **2017**, 121, 035304.
- [32] S. Olthof, K. Meerholz, *Sci. Rep.* **2016**, 7, 40267.
- [33] J. Emará, T. Schnier, N. Pourdavoud, T. Riedl, K. Meerholz, S. Olthof, *Adv. Mater.* **2016**, 28, 553.
- [34] S. Béchu, M. Ralaivisoa, A. Etcheberry, P. Schulz, *Adv. Energy Mater.* **2020**, 10, 1904007.
- [35] M. Kollár, L. Čirić, J. H. Dil, A. Weber, S. Muff, H. M. Ronnow, B. Náfrádi, B. P. Monnier, J. S. Luterbacher, L. Forró, E. Horváth, *Sci. Rep.* **2017**, 7, 1.
- [36] M. F. Yang, J. P. Yang, *Appl. Phys. Lett.* **2020**, 117, 071602.
- [37] M. Iwashita, S. Yamanaka, R. Tsuruta, K. Tonami, K. Yoshida, K. Hayakawa, L. Cojocar, S. Uchida, K. Mase, Y. Nakayama, *Appl. Phys. Lett.* **2020**, 116, 223902.
- [38] C. M. Sterling, C. Kamal, G. J. Man, P. K. Nayak, K. A. Simonov, S. Svanstrom, A. Garcia-Fernandez, T. Huthwelker, U. B. Cappel, S. M. Butorin, H. Rensmo, M. Odelius, *J. Phys. Chem. C* **2021**, 125, 8360.
- [39] G. J. Man, C. Sterling, C. Kamal, K. A. Simonov, S. Svanström, J. Acharya, F. O. L. Johansson, E. Giangrisostomi, R. Ovsyannikov, T. Huthwelker, S. M. Butorin, P. K. Nayak, M. Odelius, H. Rensmo, G. J. Man, C. M. Sterling, C. Kamal, K. A. Simonov, S. Svanström, J. Acharya, F. O. L. Johansson, E. Giangrisostomi, R. Ovsyannikov, T. Huthwelker, S. M. Butorin, P. K. Nayak, M. Odelius, H. Rensmo, *Physical Review B* **2021**, 104, 4.
- [40] F. Zu, P. Amsalem, D. A. Egger, R. Wang, C. M. Wolff, H. Fang, M. A. Loi, D. Neher, L. Kronik, S. Duhm, N. Koch, *J. Phys. Chem. Lett.* **2019**, 10, 601.
- [41] J. P. Yang, M. Meissner, T. Yamaguchi, X. Y. Zhang, T. Ueba, L. W. Cheng, S. Ideta, K. Tanaka, X. H. Zeng, N. Ueno, S. Kera, *Sol. RRL* **2018**, 2, 1800132.
- [42] M. Lee, A. Barrag, M. N. Nair, V. L. R. Jacques, A. Mattoni, A. Filippetti, C. Caddeo, *J. Phys. D: Appl. Phys.* **2017**, 50, 26LT02, 1.
- [43] A. García-Fernández, E. J. Juárez-Pérez, S. Castro-García, M. Sánchez-Andújar, L. K. Ono, Y. Jiang, Y. Qi, *Small Methods* **2018**, 2, 1800242.
- [44] C. Dong, Z. K. Wang, L. S. Liao, *Energy Technol.* **2020**, 8, 1900804.
- [45] Q. Wei, B. Shen, Y. Chen, B. Xu, Y. Xia, J. Yin, Z. Liu, *Mater. Lett.* **2017**, 193, 101.
- [46] R. Lindblad, N. K. Jena, B. Philippe, J. Oscarsson, D. Bi, A. Lindblad, S. Mandal, B. Pal, D. D. Sarma, O. Karis, H. Siegbahn, E. M. J. Johansson, M. Odelius, H. Rensmo, *J. Phys. Chem. C* **2015**, 119, 1818.
- [47] S. Svanström, A. García-Fernández, T. Sloboda, T. J. Jacobsson, H. Rensmo, U. B. Cappel, *Phys. Chem. Chem. Phys.* **2021**, 23, 12479.
- [48] T. J. Jacobsson, J. P. Correa-Baena, E. H. Anaraki, B. Philippe, S. D. Stranks, M. E. F. Bouduban, W. Tress, K. Schenk, J. Teuscher, J. E. Moser, H. Rensmo, A. Hagfeldt, *J. Am. Chem. Soc.* **2016**, 138, 10331.
- [49] H. Xie, X. Liu, L. Lyu, D. Niu, Q. Wang, J. Huang, Y. Gao, *J. Phys. Chem. C* **2016**, 120, 215.

- [50] B. Conings, J. Drijkoningen, N. Gauquelin, A. Babayigit, J. D. Haen, L. D. Olieslaeger, A. Ethirajan, J. Verbeeck, J. Manca, E. Mosconi, F. De Angelis, H. Boyen, *Adv. Energy Mater.* **2015**, *5*, 1500477.
- [51] P. Fassl, V. Lami, A. Bausch, Z. Wang, M. T. Klug, H. J. Snaith, Y. Vaynzof, *Energy Environ. Sci.* **2018**, *11*, 3380.
- [52] Z. Hawash, S. R. Raga, D. Son, L. K. Ono, N. Park, Y. Qi, *J. Phys. Chem. Lett.* **2017**, *8*, 3947.
- [53] W. Xu, L. Liu, L. Yang, P. Shen, B. Sun, J. A. Mcleod, *Nano Lett.* **2016**, *16*, 4720.
- [54] T. G. Kim, W. Seo, H. Kwon, J. Won, *Phys. Chem. Chem. Phys.* **2015**, *17*, 24342.
- [55] M. P. Seah, W. A. Dench, *Surf. Interface Anal.* **1979**, *1*, 2.
- [56] T. J. Jacobsson, S. Svanström, V. Andrei, J. P. H. Rivett, N. Kornienko, B. Philippe, U. B. Cappel, H. Rensmo, F. Deschler, G. Boschloo, *J. Phys. Chem. C* **2018**, *122*, 13548.
- [57] P. R. Varadwaj, A. Varadwaj, H. M. Marques, K. Yamashita, *Sci. Rep.* **2019**, *9*, 1.
- [58] M. Senno, S. Tinte, *Mater. Today: Proc.* **2019**, *14*, 181.
- [59] S. Tanuma, C. J. Powell, *Surf. Interface Anal.* **1994**, *21*, 165.
- [60] A. Poglitsch, D. Weber, *J. Chem. Phys.* **1987**, *87*, 6373.
- [61] B. Philippe, T. J. Jacobsson, J.-P. Correa-Baena, N. K. Jena, A. Banerjee, S. Chakraborty, U. B. Cappel, R. Ahuja, A. Hagfeldt, M. Odelius, *J. Phys. Chem. C* **2017**, *121*, 26655.
- [62] C. J. Yu, *J Phys Energy* **2019**, *1*, 022001.
- [63] T. Ida, M. Ando, H. Toraya, *J. Appl. Crystallogr.* **2000**, *33*, 1311.
- [64] A. Herrera-Gomez, M. Bravo-Sanchez, F. S. Aguirre-Tostado, M. O. Vazquez-Lepe, *J. Electron Spectrosc. Relat. Phenom.* **2013**, *189*, 76.
- [65] J. J. Yeh, I. Lindau, *At. Data Nucl. Data Tables* **1985**, *32*, 1.
- [66] M. Schmid, H. P. Steinrück, J. M. Gottfried, *Surf. Interface Anal.* **2014**, *46*, 505.
- [67] M. Campoy-quiles, O. J. Weber, J. Yao, D. Bryant, M. T. Weller, J. Nelson, A. Walsh, V. Schilfgaarde, P. R. F. Barnes, *Nanoscale* **2016**, *8*, 6317.
- [68] S. Tanuma, C. J. Powell, D. R. Penn, *Surf. Interface Anal.* **2003**, *35*, 268.
- [69] C. C. Stoumpos, C. D. Malliakas, M. G. Kanatzidis, *Inorg. Chem.* **2013**, *52*, 9019.
- [70] J. Hutter, M. Iannuzzi, F. Schiffrmann, J. Vandevondele, *Wiley Interdiscip. Rev. Comput.* **2014**, *4*, 15.
- [71] C. Caddeo, M. I. Saba, S. Meloni, A. Filippetti, A. Mattoni, *ACS Nano* **2017**, *11*, 9183.
- [72] S. Nosé, *J. Chem. Phys.* **1984**, *81*, 511.
- [73] G. J. Martyna, M. L. Klein, M. Tuckerman, *J. Chem. Phys.* **1992**, *97*, 2635.
- [74] W. G. Hoover, *Phys. Rev. A* **1985**, *31*, 1695.
- [75] K. Momma, F. Izumi, *J. Appl. Crystallogr.* **2011**, *44*, 1272.
- [76] M. Iannuzzi, J. Hutter, *Phys. Chem. Chem. Phys.* **2007**, *9*, 1599.
- [77] J. P. Perdew, K. Burke, M. Ernzerhof, *Phys. Rev. Lett.* **1996**, *77*, 3865.
- [78] S. Grimme, J. Antony, S. Ehrlich, H. Krieg, *J. Chem. Phys.* **2010**, *132*, 154104.
- [79] A. Allouche, *J. Comput. Chem.* **2012**, *32*, 174.
- [80] S. Goedecker, M. Teter, *Phys. Rev. B* **1996**, *54*, 1703.
- [81] M. Krack, *Theor. Chem. Acc.* **2005**, *114*, 145.
- [82] J. Vandevondele, J. Hutter, *J. Chem. Phys.* **2007**, *127*, 114105.
- [83] G. Lippert, J. Hutter, M. Parrinello, *Mol. Phys.* **1997**, *92*, 477.